Spontaneous Formation of Nanopatterns in Velocity-Dependent Dip-Coated Organic Films: From Dragonflies to Stripes

Tomas P. Corrales,[†,▲,▽] Mengjun Bai,[‡,▽] Valeria del Campo,[†,∞] Pia Homm,[†] Piero Ferrari,[†] Armand Diama,[‡,§] Christian Wagner,[∥] Haskell Taub,[‡] Klaus Knorr,[∥] Moshe Deutsch,[#] Maria Jose Retamal,[¶] Ulrich G. Volkmann,[¶] and Patrick Huber[*,†,∥,△]

[†]Facultad de Física, Pontificia Universidad Católica de Chile, 7820436 Santiago, Chile, [‡]Department of Physics and Astronomy, University of Missouri, Columbia, Missouri 65211, USA, [∥]Experimental Physics, Saarland University, D-66041 Saarbruecken, Germany, [#]Physics Department and Institute of Nanotechnology and Advanced Materials, Bar-Ilan University, Ramat-Gan 52900, Israel, [¶]Instituto de Física and Centro de Investigación en Nanotecnología y Materiales Avanzados (CIEN-UC), Facultad de Física, Pontificia Universidad Católica de Chile, 7820436 Santiago, Chile, and [△]Institute of Materials Physics and Technology, Hamburg University of Technology (TUHH), D-21073 Hamburg-Harburg, Germany. [▽]These authors contributed equally to this work. [▲]Present address: Department of Physics, Laboratory of Atomic and Solid State Physics, Cornell University, Ithaca, New York 14853, USA. [§]Present address: Laboratoire de Physique de la Matière Condensée et de Technologie LPMCT, Université de Cocody, Abidjan, Côte d'Ivoire. [∞]Present address: Departamento de Física, Universidad Técnica Federico Santa María, 2391206 Valparaíso, Chile.

ABSTRACT We present an experimental study of the micro- and mesoscopic structure of thin films of medium length *n*-alkane molecules on the native oxide layer of a silicon surface, prepared by dip-coating in a *n*-$C_{32}H_{66}$/*n*-heptane solution. Electron micrographs reveal two distinct adsorption morphologies depending on the substrate withdrawal speed *v*. For small *v*, dragonfly-shaped molecular islands are observed. For a large *v*, stripes parallel to the withdrawal direction are observed. These have lengths of a few hundred micrometers and a few micrometer lateral separation. For a constant *v*, the stripes' quality and separation increase with the solution concentration. Grazing incidence X-ray diffraction and atomic force microscopy show that both patterns are 4.2 nm thick monolayers of fully extended, surface-normal-aligned alkane molecules. With increasing *v*, the surface coverage first decreases then increases for $v > v_{cr} \sim 0.15$ mm/s. The critical v_{cr} marks a transition between the evaporation regime, where the solvent's meniscus remains at the bulk's surface, and the entrainment (Landau–Levich–Deryaguin) regime, where the solution is partially dragged by the substrate, covering the withdrawn substrate by a homogeneous film. The dragonflies are single crystals with habits determined by dendritic growth in prominent 2D crystalline directions of randomly seeded nuclei assumed to be quasi-hexagonal. The stripes' strong crystalline texture and the well-defined separation are due to an anisotropic 2D crystallization in narrow liquid fingers, which result from a Marangoni flow driven hydrodynamic instability in the evaporating dip-coated films, akin to the tears of wine phenomenology.

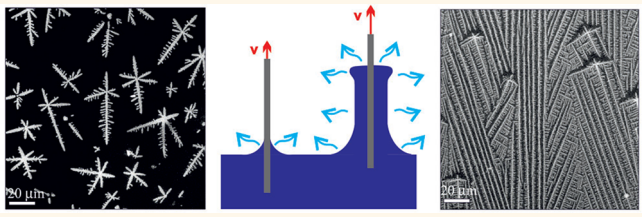

KEYWORDS: 2D crystallization · Marangoni flows · *n*-alkane · silicon · atomic force microscopy · scanning electron microscopy · X-ray diffraction

A moving liquid/solid/air triple line of a volatile liquid, omnipresent in dip-coating processes, exhibits a remarkably complex, non-equilibrium physics: The hydrodynamic shear stress and evaporation rate diverge according to theoretical models.[1−3] The latent heat of evaporation (and sometimes crystallization) induces temperature inhomogeneities and concentration gradients which cause an interplay of interfacial and gravitational forces, evaporation, diffusion, and thin-film flows which can lead to patterned coatings. The underlying pattern formation processes are of fundamental interest.[4] Their control allows one to form self-assembled, patterned thin-film structures over large areas,[5−7] which are of relevance in many nanotechnological fields, ranging from surface wettability control[8−10] and supported biomembranes[11] to organic electronics.[12,13]

* Address correspondence to patrick.huber@tuhh.de.

Received for review March 14, 2014 and accepted September 4, 2014.

Published online September 04, 2014
10.1021/nn5014534

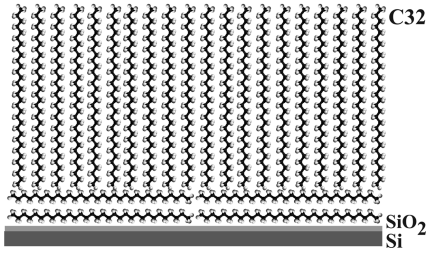

Figure 1. Schematic side view of the microscopic structure of thin C32 films on the native oxide layer of a silicon substrate.

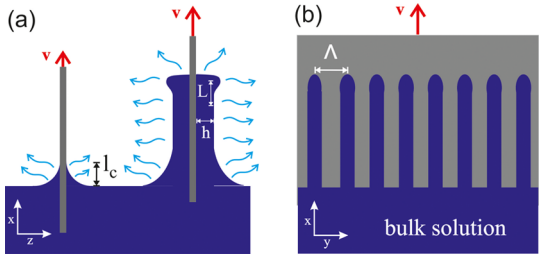

Figure 2. Schematics of the dip-coating geometry: (a) side view of the evaporation (left) and the entrainment (Landau–Levich–Deryaguin) (right) regimes; (b) top view in the Landau–Levich–Deryaguin regime, after the Marangoni flow-driven hydrodynamic instability induces fingers in the evaporating dip-coated film. The *x*, *y*, and *z* are, respectively, the directions of withdrawal, solution/substrate/air contact line, and the surface normal. The meniscus height, which for slow speeds and small contact angles agrees with the capillary length l_c, is shown in (a). *L*, Λ, and *h* are, respectively, the characteristic length of the advancing liquid bulb, the wavelength of the fingering instability, and the coating film thickness in the Landau–Levich–Deryaguin regime, discussed in the text.

These interesting fundamental and technological aspects of pattern formation in the dip-coating of molecular[14−18] and colloidal solutions,[19−21] as well as our own observation a few years ago of stripe formation in the dip-coating of silicon wafers by alkane solutions, are the motivation for this study.

Normal alkanes, such as dotriacontane (n-$C_{32}H_{66}$ denoted C32) studied here, are basic building blocks of complex organic molecules like lipids, surfactants, and liquid crystals[22] and exhibit a remarkably rich bulk[23] and surface phase behavior.[24−28] Spatially confined in pores or capsules[29−33] or semi-infinitely confined on planar substrates, such as silicon,[34] sapphire,[35] and graphitic surfaces,[36,37] they constitute important examples of soft molecular systems meeting classic solids.

The structure and thermodynamics of *n*-alkanes on silica (SiO_2)-terminated silicon wafers[34,38−45] have been extensively studied, with C32 providing the most detailed insights. High-resolution ellipsometry,[34] atomic force microscopy (AFM),[41,43] and both X-ray reflectivity[40,46] and grazing incidence X-ray diffraction (GIXD)[41] revealed that C32 films are composed of two layers, in which the molecules are oriented parallel to the SiO_2 surface. Above this bilayer, molecules organize in layers with their long axis oriented perpendicular to the surface, as shown in Figure 1. Laterally, the molecules form a quasi-hexagonal, 2D rectangular lattice, which results in an orthorhombic crystalline structure with lattice parameters a = 7.57 Å, b = 4.98 Å, and c = 85.0 Å at room temperature.[40,41]

In this work, we examine the micro- and mesoscopic structure formation occurring upon dip-coating of silicon wafers in C32/*n*-heptane solutions (see Figure 2). The morphological evolution as a function of withdrawal speed v is related to both the dynamical processes occurring at the three-phase solution/substrate/air contact line and the crystallization mechanisms in the 2D films.

RESULTS

Figure 3 presents scanning electron microscopy (SEM) images of samples drawn at v ranging from 0.03 mm/s (a) to 1 mm/s (f). For $v \leq 0.17$ mm/s, the molecules form islands with a dendritic morphology, as reported in ref 41 and denoted as dragonfly structures, shown magnified in Figure 4. Above $v \approx 0.25$ mm/s, the length of the dragonfly's long axis increases, particularly in the withdrawal direction, and the long axes increasingly tend to align parallel to this direction. At 1 mm/s, this leads to the formation of an almost perfect parallel stripe pattern inclined or parallel to the withdrawal direction.

In the AFM images (Figures 5 and 6), the well-defined stripe pattern is also clearly observable. The height of the stripes (see bottom panel in Figure 6) is ∼4.2 nm as measured in the AFM contact mode.[47] Because this value agrees with the length of a single all-*trans* C32 molecule (see Figure 1), it indicates that the C32 molecules are aligned perpendicular to the substrate plane. This conclusion is in good agreement with previous ellipsometry and X-ray reflectivity measurements, which also showed that below the perpendicular molecules is a homogeneous bilayer of parallel molecules[40,46] (see Figure 1).

Obviously, the C32 surface coverage and the quality of the stripe pattern in the AFM picture of Figure 6 are markedly higher than those in the SEM pictures depicting stripes (see Figure 3). These originate in the difference in the C32 solution concentrations used for the sample preparation. As documented in the sequence of AFM images in Figure 5 documents, recorded for a fixed v = 1 mm/s, the monolayer coverage and the quality of the stripe pattern increase markedly with increasing concentration.

The distinct morphological changes in the alkane coating are accompanied by substantial changes in the v-dependent surface coverage $C(v)$. To quantify this, the SEM images were divided into areas covered (white) and not covered (black) by a layer of substrate-normal molecules. C then corresponds to the percentage of white pixels in the image, plotted in Figure 7. $C(v) > 50\%$

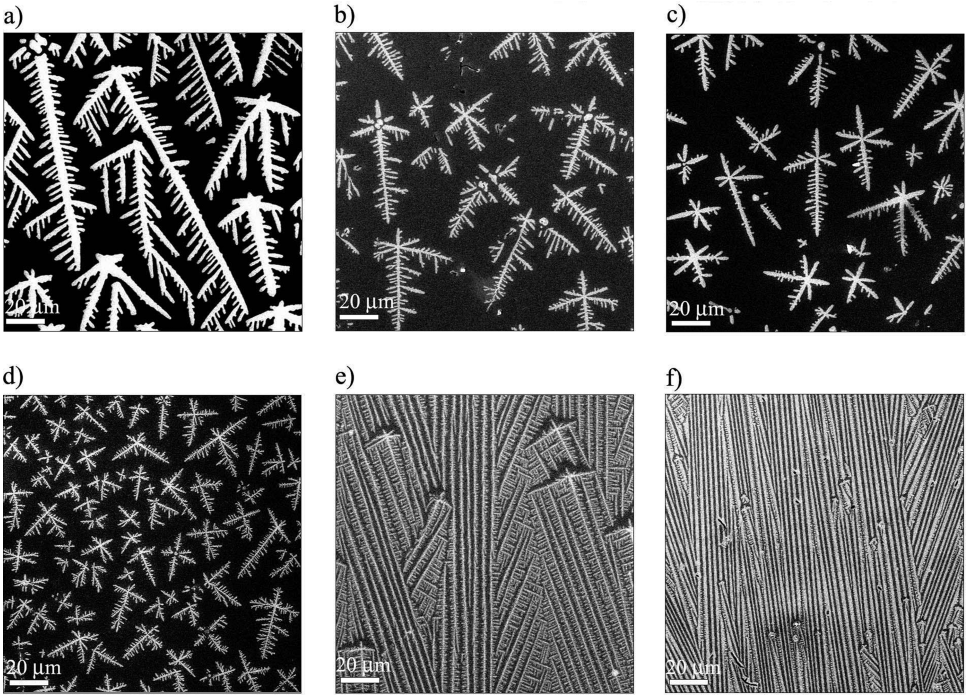

Figure 3. Electron micrographs of a C32 film morphology for *v* of (a) 0.03 mm/s, (b) 0.08 mm/s, (c) 0.17 mm/s, (d) 0.25 mm/s, (e) 0.5 mm/s, and (f) 1 mm/s. The C32 solution concentration is 1.81 mmol/L.

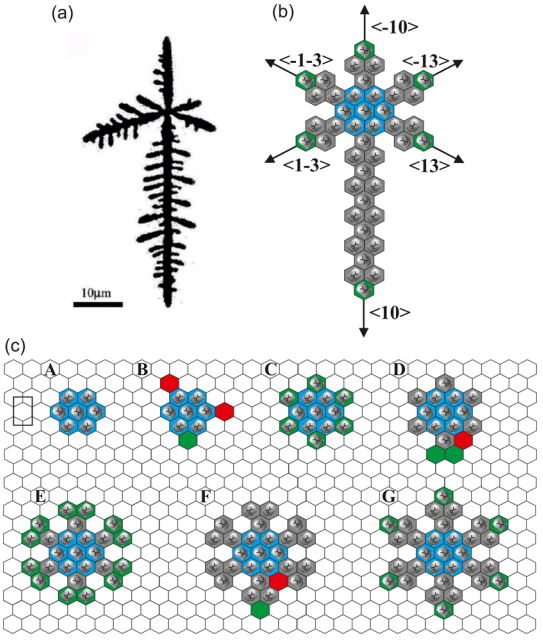

Figure 4. (a) Electron micrograph of a "dragonfly" cluster for *v* = 0.17 mm/s and C32 solution concentration of 1.81 mmol/L. (b) Dragonfly 2D crystallography: the filled hexagons (top views of the page-normal C32 backbones) represent possible lateral C32 positions in a 2D quasi-hexagonal, rectangular lattice. (c) Illustration of a sequential, dendritic growth mechanism resulting in the dragonfly morphology. Green and red hexagons represent, respectively, favored and unfavored attachment sites for growth. See text for discussion.

at very small *v* decreases rapidly with increasing *v*. At 0.17 mm/s, only 10% of the surface is covered. However, as *v* increases further, $C(v)$ also increases, reaching a plateau of 35% at $v \approx 1$ mm/s.

The direct imaging methods presented above give some insights into the meso- and macroscopic morphology. However, surface-sensitive X-ray diffraction allows one to uncover the microscopic details of the molecular order within the film. Figure 8a,b shows, respectively, the scattering geometry and two diffraction patterns for a striped sample at two azimuthal sample orientations, $\omega = 0$ and 55°. The peaks observed in (b) are attributable to the (11) and (20) Bragg reflections from a 2D rectangular lattice with $a = 7.57$ Å and $b = 4.98$ Å, that is, $q_{11} = 1.51$ Å^{-1} and $q_{20} = 1.67$ Å^{-1}, in good agreement with the structure of the crystalline C32 monolayer reported in the literature.[41] Note that, for presentation reasons, $\omega = 0°$ was chosen at the azimuthal orientation maximizing the intensity of the (20) reflection. This occurs at ~6° relative to its initial orientation with the incident beam perpendicular to the stripe or *x* direction. This rotation agrees reasonably well with the Bragg angle $\theta = 5.8°$ of the (20) reflection.

Both the (11) and the (20) Bragg peaks are asymmetric and exhibit shoulders. This could indicate the coexistence of structures with slightly different lattice constants or an oblique 2D mesh, for example, in order to achieve commensurability with the underlying flat-lying molecules. These effects have been observed for *n*-alkanes on crystalline substrates.[48,49] A lattice constant spread could also originate in the variation of the hydrodynamic shear stresses encountered by the crystals during the non-equilibrium growth processes. In addition, the instrumental resolution and the finite grain sizes contribute to the peak broadening.[50]

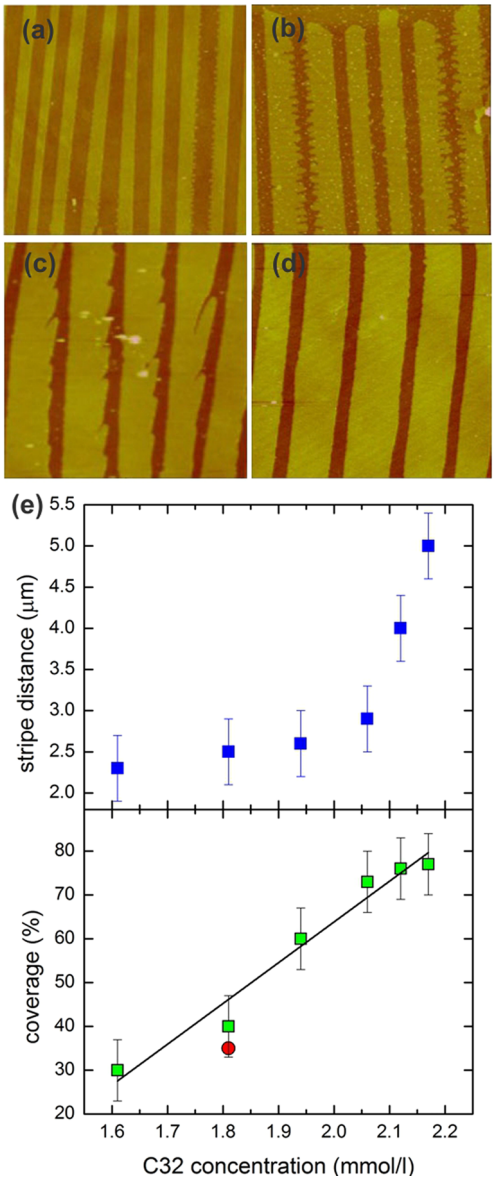

Figure 5. AFM topography images of samples manually withdrawn at $v \approx 1$ mm/s from C32 solutions at concentrations of (a) 1.81 mmol/L, (b) 1.94 mmol/L, (c) 2.12 mmol/L, and (d) 2.17 mmol/L. Image widths are 20 μm. (e) Concentration dependence of substrate coverage and stripe width for $v = 1$ mm/s as determined from AFM pictures (squares). Coverage determined from a SEM image at $v = 1$ mm/s is shown for comparison (red circle). The solid line is a linear fit to the AFM points.

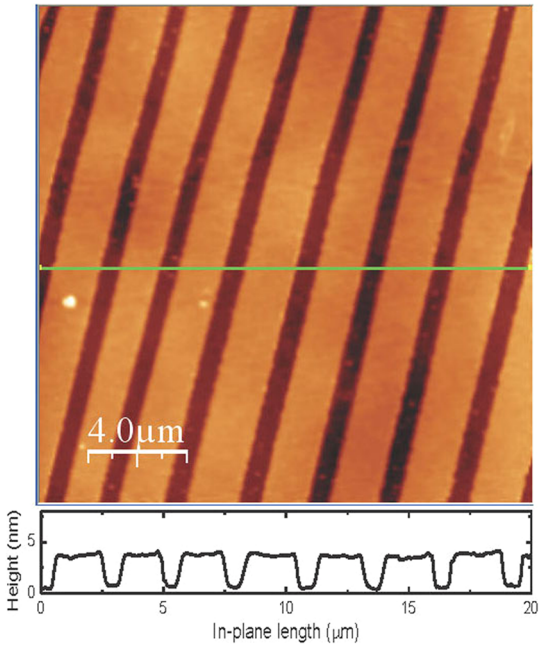

Figure 6. AFM topography image of a sample manually withdrawn at $v \approx 1$ mm/s from a solution with a C32 concentration of 2.06 mmol/L. Bottom panel: height profile along the line in the top panel. Coverage is 74%.

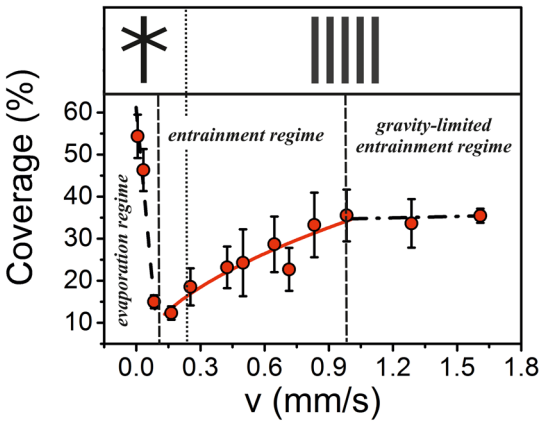

Figure 7. Dependence of v on the surface coverage by C32 for a solution concentration of 1.81 mmol/L. The solid and dashed lines correspond to characteristic scaling regimes discussed in the text. As illustrated in the top panel, the vertical dotted line marks the velocity of ~0.25 mm/s separating the regimes of dragonfly and stripe formation.

Our experimental data are, however, insufficiently detailed to separate those effects. Therefore, we resort to the simple 2D lattice suggested above because it describes reasonably well all our experimental findings and conjectures outlined below.

Clearly, the 2D diffraction patterns of Figure 8b are not a powder average of randomly oriented crystals. The finding that only the (20) reflection is observable for $\omega = 0°$ and only the (11) reflection is observable for $\omega = 55°$ indicates a strong crystalline texture. This conclusion is supported by the pole figure depicted in Figure 8c, where the intensity variation of these two prominent 2D peaks is plotted as a function of the azimuthal angle ω. The (20) reflection appears only close to $\omega = 0$ and 180°, indicating that the ⟨10⟩ direction (the a direction of the rectangular lattice) is almost perfectly aligned with the stripe and withdrawal (x) direction. Furthermore, the peaking of the (11) reflections' intensity in the pole figure at $\omega_{11} = 55.7°$ and $\omega_{\bar{1}1} = 122.9°$ agrees reasonably well with this ⟨10⟩ orientation.

Note, however, that the peaks in the pole figure exhibit sizable ω widths of ~10° fwhm, significantly

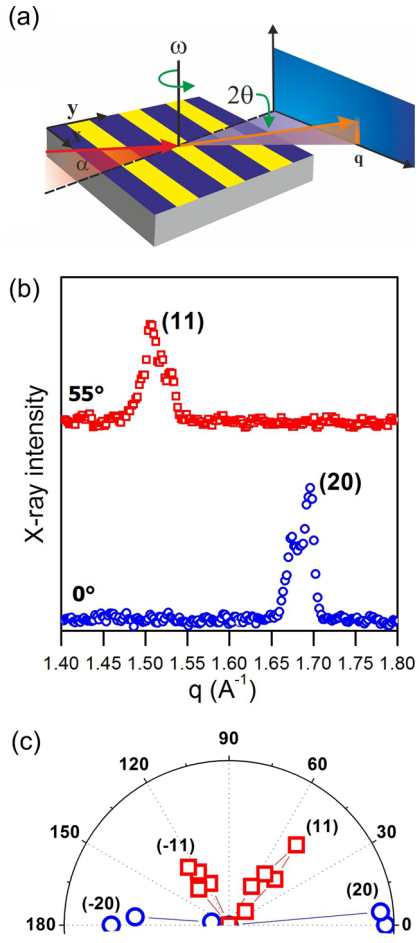

Figure 8. GIXD measurements. (a) Schematic diagram of the scattering geometry; α, ω, and 2θ are, respectively, the X-rays' incidence angle, the sample's azimuthal rotation angle, and the scattering angle. (b) Diffraction patterns of a striped sample at the two indicated ω orientations. (c) Overlay of two pole diagrams, *i.e.*, peak intensity positions in ω, measured in 5° steps at two fixed Bragg angles, 2θ = 10.55° (squares) and 11.67° (circles), corresponding to the (11) and (20) reflections at q_{11} = 1.51 Å^{-1} and q_{20} = 1.67 Å^{-1}, respectively; ω = 0 is ~6° rotated from the direction, where *x*, the withdrawal (and stripe) direction, is perpendicular to the incident beam. The sample was prepared from a solution with a C32 concentration of 2.06 mmol/L.

above the estimated experimental ω resolution of ~1°. This observation indicates either a large crystalline mosaicity within the stripes or a significant angular distribution of the orientation of single-crystalline stripes around the withdrawal direction. The SEM pictures of Figure 3f clearly support the idea of such a broad azimuthal distribution of the stripe orientations. Hence, we attribute the large peak width in the pole figure to the imperfect alignment of the stripes rather than to mosaicity. Of course, we cannot exclude a superposition of both effects, which can only be verified by high-resolution peak shape measurements[50] currently unavailable.

DISCUSSION

First, one may ask whether the C32 adsorption is complete prior to the withdrawal of the substrate. A previous ellipsometry study[51] found no evidence for such a layer, implying a concentration below that required for layer formation, c_l. Thus, the layers of surface-normal molecules discussed above must form upon wafer withdrawal from the solution. This also explains why the morphology of the adsorbate is entirely independent of the immersion time but is very sensitive to the withdrawal speed. The physics involved is that of the forced wetting of a substrate pulled out of a bulk liquid as pioneered by Landau, Levich,[52] and Deryaguin,[53] extended by de Gennes[54] and Eggers,[55,56] and reviewed in refs 3 and 57.

The geometry of the withdrawal is shown in Figure 2. In the static case (v = 0 mm/s withdrawal speed along $+x$), a (curved) meniscus forms due to the competition of gravity, g, and surface tension, γ. The contact angle at the contact line is somewhere between 0 and 90°. The meniscus's characteristic x length is, in the present case, on the order of the capillary length $l_c = (\gamma/\rho g)^{1/2}$, where ρ is the liquid's mass density. For dip-coating with a finite velocity v (forced wetting), this meniscus is deformed, stretched along the $+x$ direction into a dynamical meniscus. Its extension depends on a competition between the liquid capillary force upward and the gravitational force downward. The no-slip velocity boundary condition at the liquid/substrate interface along with the fluid's inertia and the viscous forces favors the formation of a liquid film on the withdrawn part of the substrate. Solving the Navier−Stokes equation for this situation yields a critical velocity v_{cr} below which no liquid film forms on the substrate (regime I or evaporation regime). Above v_{cr}, a film is formed whose thickness depends sensitively on the withdrawal velocity (regime II, entrainment or Landau−Levich−Deryaguin (LLD) regime).

A quantitative analysis yields for the critical velocity, v_{cr}, separating these two regimes for an ideal, planar substrate withdrawn vertically from a bulk solution (eq 9 in ref 55)

$$Ca_{cr} = \frac{\theta_e^3}{9}\frac{1}{A(\gamma, \eta, H, Ca_{cr})} \qquad (1)$$

where $Ca_{cr} = v_{cr}\eta/\gamma$ is the capillary number (the ratio of viscous to surface forces) at v_{cr}, θ_e is the static contact angle, η the viscosity, and $A(\gamma, \eta, H, Ca_{cr})$ is a logarithmic correction that depends on the fluid parameters and the Hamaker constant typical of the solution/substrate van der Waals interaction.

The distinct film formation regimes imply distinct scaling regimes for $C(v)$. As shown below, in the evaporation regime, the amount of deposited material monotonically decreases whereas in the LLD regime it monotonically increases with v. Thus, a surface coverage minimum is expected in dip-coating at v_{cr} and is indeed observed at $v \sim 0.15$ mm/s in Figure 7. When the influence of the solute is neglected and the fluid parameters of pure C7 used (γ = 20.14 mN/m,

η = 0.42 mPas, $H = 5 \times 10^{-20}$ J),[57] v = 5 mm/s corresponds through eq 1 to a contact angle of $\theta_e \approx 3.5°$. We are not aware of any θ_e measurements of C7 on silica surfaces with sufficiently high precision. The small value of θ_e agrees well with the almost perfect wetting and spreading behavior reported for *n*-heptane on silica surfaces.[57,58]

The formation of the dragonfly-shaped molecular islands in regime I (v < 0.15 mm/s) can now be rationalized as follows: The C7 evaporation in the stationary meniscus leads to concentrations exceeding c_I. Initially, the supersaturation is low. Nucleation centers of the monolayer of surface-normal molecules are formed, and growth proceeds under equilibrium conditions. Faceted 2D crystals with quasi-hexagonal habits are formed, reminiscent of the crystalline structure of the surface-frozen monolayer forming at the free surface of a bulk C32 melt.[25,26] These constitute the dragonflies' nucleation centers shown in Figure 4. With a further increase in supersaturation, dendritic growth sets in.[59] The molecules are preferentially attached in the fast-growing ⟨10⟩ and ⟨$\bar{1}$0⟩ in-plane directions (*a* directions of the 2D in-plane lattice),[30] which form the dragonfly's body, and the (⟨13⟩,⟨$\bar{1}$3⟩,⟨1$\bar{3}$⟩,⟨$\bar{1}\bar{3}$⟩) directions, which form its four wings (see Figure 4). Note that the angle between the ⟨10⟩ direction and the set of ⟨13⟩ directions is 63°, in good agreement with the corresponding angle in the electron micrographs shown in Figure 4.

The dendritic growth directions leading to the dragonfly shape can be traced to basic 2D crystallization principles of a quasi-hexagonal packing, the dominant 2D interactions between the fully extended hydrocarbon backbones, and the peculiar self-assembly conditions in the confined geometry of the evaporating meniscus. First, the isotropic part of the van der Waals interaction between extended C32 molecules drives a triangular packing of the molecules. The quadrupolar contribution favors perpendicular backbone planes for neighboring hydrocarbons, leading to a herringbone ordering of the hydrocarbon backbones and a slight distortion of the hexagonal arrangement.[29,60−62] Thus, the basic 2D crystal nucleus is quasi-hexagonal with a herringbone ordering of the C32 backbones, as shown in A in Figure 4c. The preference for a triangular packing, that is, being at a vertex of a triangle, drives the next molecule that joins the nucleus to a position fulfilling this condition, as shown in green in B. Now, the 2D crystallite formation (shown in C) depletes the local alkane concentration, which is low anyway. So, the next molecules to join the crystal have to come in from some distance away from the center of the growing crystal. Coming in, they will first meet the outermost reach of the crystal, positions like those marked in green in D. To reach positions closer to the center, like that in red in D, they will need to diffuse further in. So, the molecules attach to the first suitable position they meet (i.e., the green one), but because they prefer triangular packing, two molecules will attach, as shown in green in D, creating the crystal in E. This makes the red position in F even less accessible to molecules, rendering attachment of molecules there in further growth steps even less likely. The next step proceeds similarly to that from A to C, creating G from E. Repeating this process creates the dragonfly-shaped crystallite shown in Figure 4b.

The herringbone packing, distorting the hexagons in the crystallographic *a* direction, reduces the nearest neighbor distances in this direction and increases the molecular attraction. Thus, the free-energy gain in a molecular attachment is larger in this direction than in the ⟨13⟩ directions. The crystallite grows, therefore, preferentially along the ⟨10⟩ direction, yielding the longer dragonfly body in Figure 4b.

The scenario above implies that the dragonflies are single crystals, similar to many types of dendritically grown snowflakes.[63] This conclusion is supported by the observation that all wings of second (or higher) order have a fixed angular relation to the main body and the wings of first order, as observed in Figure 4a. X-ray diffraction on these crystallites, currently unavailable, is required to conclusively validate this point. Their microscopic architecture has been indirectly inferred from the mesoscopic morphology and the known 2D crystalline structure of the monolayer. Therefore, we cannot exclude an additional influence on the dragonfly morphology due to a crystalline arrangement of the underlying parallel bilayer. Moreover, the growth scenario is only qualitative and does not describe the full details of the crystallization process and the structure of the growing dragonfly. Similarly, as demonstrated for crystal nucleation and growth of bulk alkane crystals,[64−67] computer simulations could provide important complementary insight.

The number of dragonfly nucleation centers increases with the time that the meniscus is in contact with the substrate, decreases with the solvent concentration, and depends on the evaporation rate and the flow profiles in the meniscus. Considering the flow profile in the receding meniscus, Berteloot *et al.*[4] recently predicted the existence of a stagnation zone where the net liquid flux vanishes over a distance l_d from the triple line with l_d proportional to v^2. If we assume that all of the solute up to the distance l_d is deposited on the substrate and that the solute concentration in that volume is uniform and equals the bulk concentration, $C(v)$ should decay monotonically as v^{-2}.[4] Le Berre *et al.*[16] and Rogowski and Darhuber[17] suggest a slightly different adsorption scenario. They consider a simple mass balance in a box surrounding the meniscus. At steady state, the solvent flow leaving the box by evaporation equals that entering it. Mass conservation requires the solute's outward flux from the film to equal the inward flux from the solution, resulting in a v^{-1} scaling of C.[16] The mass balance implies that no concentrated solution flows back into

the bulk liquid, in contrast to the Berteloot *et al.* scenario, which is considered to be more appropriate for colloidal solutions.[68] In agreement with both models, we observe a monotonic decrease in $C(v)$. However, because of the limited number of data points and the narrow v range explored, we cannot deduce any scaling law for $C(v)$ and thus corroborate one of the suggested models.

Above v_{cr}, in the LLD regime, the coverage starts to increase monotonically. For small velocities (0.17 mm/s < v < 0.25 mm/s), the dragonfly morphology dominates. Above $v \approx 0.25$ mm/s, the pattern formation mechanisms change significantly, yielding the striped phase.

In the following, we argue that this surprising change results from a hydrodynamic instability in the film coating. We discuss each of the contributing processes separately, although in reality, they all proceed simultaneously:

(i) Because $v > v_{cr}$, a constant thickness (h) film remains on the previously immersed part of the substrate with h scaling as $h \propto v^{2/3}$ on a flat, homogeneous, and completely wettable substrate.[52,53]

(ii) The C7 evaporation cools the liquid's surface. The resulting temperature drop is much larger in the meniscus and the thin film region ($x > 0$) than in the liquid away from the wafer, due to the corresponding mass ratios. Thus, a temperature gradient dT/dx develops, with the colder region at $x > 0$. This is accompanied by a C32 concentration gradient, dc/dx, due to evaporation. Since the high-surface-tension solute (γ(C32) = 28 mN/m > γ(C7) = 20 mN/m) is enriched at $x > 0$ and the surface tension increases with decreasing temperature, both gradients are positive and sum up to a positive gradient of the surface tension ($d\gamma/dx = \partial\gamma/\partial T \times dT/dx + \partial\gamma/\partial c \times dc/dx$).

(iii) The $d\gamma/dx$ implies a Marangoni surface stress, $\tau = d\gamma/dz$. This surface stress results in a liquid flow in the direction of higher surface tension, that is, parallel to the $+x$ direction, opposing the viscous forces. This phenomenology has been nicely demonstrated experimentally by Cazabat *et al.*[69,70] Liquid piles up, forming a ridge along y, at the advancing contact line (see Figure 2). This "bump" is unstable and breaks up into fingers (see Figure 6), in a manner similar to the Rayleigh−Plateau instability, which causes a column of fluid to break up into droplets or the formation of liquid fingers during dewetting of thin films.[71] The resulting liquid stripes (and uncovered substrate regions) are parallel to the withdrawal direction, an effect akin to the famous "tears of wine".[72]

As first suggested by Huppert,[73] the characteristic wavelength Λ of this fingering instability is determined by the length of the capillary region at the advancing liquid bulb L, where the capillary force is comparable to the viscous and Marangoni forces. Our Λ is a few micrometers and monotonically decreases with increasing v. For v = 0.25, 0.5, and 1.0 mm/s, we observe Λ = 4, 2.6, and 2.3 μm, respectively. Also, as demonstrated by AFM (Figure 5), not only the coverage increases monotonically with concentration but also Λ increases significantly. Unfortunately, no information is available on the velocity of the Marangoni stress induced upward movement of the liquid bulb, which could allow us to calculate L[69,70,74] and relate it to the Λ observed.

Within the liquid stripes, c_l is soon reached due to evaporation, and thus the formation of the 2D surface-normal C32 layer sets in. The growth is again dendritic, and there is a competition of the purely hydrodynamically dictated perpendicular stripe formation and the dendritic growth, which is governed by the fast 2D crystallization directions, in particular, the ⟨10⟩ or a direction, already discussed with regard to the dragonfly morphology. Therefore, the stripes are preferentially, but not perfectly, aligned with the withdrawal direction and highly textured with a dominant alignment of the ⟨10⟩ direction along the stripe direction as inferred from the GIXD measurements. There is also dendritic growth at the stripe edges (see Figure 3e and Figure 5), which occurs in more than one direction. Hence, the stripe formation and their crystalline textures are a rather complex interplay of crystallization in a confined geometry and the rich non-equilibrium physics encountered during the dip-coating process. The prevalence of the dragonfly pattern for low velocities, just above v_{cr}, may result from a suppression of the fingering instability due to the very small thickness of the coating film and the corresponding strong viscous damping or inhibition of Marangoni flows.

It is interesting to note that the 2D growth mechanisms described above are effective enough to absorb all molecules into the 2D structures. No 3D bulk crystallites or multilayers were observed to form in any of our measurements, implying that C32 concentrations typical for the formation of such structures are never reached.

The faster the substrate is withdrawn from solution, the thicker is the solution film formed on the substrate. Therefore, more molecules deposit onto the substrate. This explains the monotonic increase in coverage for increasing $v > v_{cr}$: Given the adsorption and growth mechanism outlined above, $C(v)$ should scale as the LLD prediction for the film thickness, $h \propto v^{2/3}$. We indeed find $C(v) \propto v^{0.60\pm0.05}$ (see red line in Figure 7), in good agreement with this prediction.

Finally, our surface coverage saturates at $v > 1$ mm/s (Figure 7). This behavior is expected because gravity eventually limits the film thickness.[15]

SUMMARY AND CONCLUSIONS

We have presented an experimental study of the micro- and mesoscopic structure of thin films of C32 on native oxide layers of silicon surfaces prepared by dip-coating. Electron micrographs reveal two distinct

coating morphologies as a function of substrate withdrawal speed v. For small v, we observe dragonfly-shaped molecular islands. For larger v, we observe stripes aligned parallel to the withdrawal direction and extending over hundreds of micrometers with a well-defined separation of a few micrometers. GIXD and AFM indicate that both the dragonflies and the stripes consist of a monolayer of fully extended, surface-normal-aligned alkane molecules. The coverage and quality of the stripe pattern increase significantly with the solution's C32 concentration for a fixed $v \approx 1$ mm/s.

The two v regimes are identified as an evaporation regime at low v, where the solution meniscus remains at the bulk's surface, and a Landau−Levich−Deryaguin entrainment regime at high v, where it is drawn upward with the substrate. The transition between the two regimes occurs at a critical $v_{cr} \approx 0.15$ mm/s. The different morphology films observed in the two regimes both consist of single crystals. In the evaporation regime, their dragonfly-shaped habit is explained by a scenario of dendritic growth based on sequential molecule attachment to preferred sites in the growing crystal nucleus. In the entrainment regime, the well-defined stripe texture is traced to a Marangoni flow-driven hydrodynamic instability in the evaporating films, akin to the tears of wine phenomenology.

In general, our study highlights the principal versatility of dip-coating processes to achieve structural control over several orders of magnitude in length scales (from the microscopic to the macroscopic length scales) and thus its suitability to prepare large-scale, hierarchically-arranged surface patterns. A more detailed experimental investigation of the initial phases of the stripe formation and a more appropriate theoretical description of this complex phenomenology would be desirable.

Finally, we would like to emphasize the robustness of the pattern formation processes studied here against possible variations of the experimental conditions, in particular, the substrate withdrawal kinetics. High-quality, homogeneous, and large-scale stripe patterns could be produced by manually withdrawing the wafers from the bulk solution, which renders the procedures documented particularly suitable for nanopatterning of surfaces with hydrocarbons on laboratory and perhaps also on industrial scales.

EXPERIMENTAL SECTION

Si(100) wafers (Virginia Semiconductor, Inc.), 0.4 mm thick and terminated by a ∼ 15 Å thick native surface oxide layer, were used as substrates. They were cleaned by immersion in a Piranha solution (70% H_2SO_4 + 30% H_2O_2) at 90 °C for 30 min. This treatment does not affect the oxide layer[75] and yielded reproducible, clean, and hydrophilic surfaces.

All dip-coating solutions for the v-dependent SEM measurements were prepared by sonicating 16 mg of C32 (Aldrich, 99% purity) in 20 mL of *n*-heptane for 15 min, yielding a 1.81 mmol/L solution. For the GIXD measurements, a slightly higher concentration, 2.06 mmol/L, was used. As these are well below the 24.7 mmol/L solubility[76] of C32 at 20 °C, full C32 dissolution is implied. Specifically, no visible light scattering typical of the formation of C32 clusters larger than 0.1 μm has been observed during the measurements and storage time (>1 week). To deposit the C32 film, the substrate was fully immersed in the solution, then withdrawn at a constant speed v, as shown in Figure 2. Withdrawal velocities were controlled in the range of 0.007 mm/s $\lesssim v \lesssim$ 1.7 mm/s by a micrometer, turned by a stepper motor.

Coverage C and morphology of the samples were measured by scanning electron microscopy (operated in high vacuum at 25 kV) immediately following sample preparation. AFM measurements were performed with a Nanoscope IIIa (Veeco Instruments Inc.) operating in the tapping mode. Commercial ultrasharp rectangular silicon cantilevers were used. Their nominal spring constant was ∼0.35 N/m, and the resonance frequency was ∼33 kHz. We recorded AFM topographic and phase images simultaneously for several concentrations from 1.81 to 2.17 mmol/L.

GIXD measurements were performed at the Advanced Photon Source (Materials Science Beamline 6-ID-B) at the Argonne National Laboratory using a synchrotron X-ray beam with a wavelength of 0.7653 Å. The incident angle α was 0.1°. An image plate detector (MAR345 with resolution of 0.150 mm/pixel) was used to record the 2D diffraction patterns. The horizontal GIXD curves were extracted and averaged vertically for 10 pixels above the strong surface enhancement peak.

Note that the AFM and GIXD samples were coated by manually withdrawing the silicon wafers from the solutions at $v \approx 1$ mm/s. The samples were kept in a dry nitrogen gas atmosphere during the AFM and GIXD measurements to protect them from contamination.

Conflict of Interest: The authors declare no competing financial interest.

Acknowledgment. Support by FONDECYT Grant No. 1100882 and 1141105, U.S. National Science Foundation Grant Nos. DMR-0411748, DMR-0705974, and DGE-1069091, and graduate school 1276 of the German Research Foundation (DFG), "Structure formation and transport in complex systems" (Saarbruecken, Germany), is gratefully acknowledged, as are scholarships to M.J.R. by CONICYT and to Pa.H., M.J.R., and U.V. by the Binational German−Chilean Academic Exchange project (German Academic Exchange Service Project No. 56206483/ CONICYT Project No. PCCI 044). The Advanced Photon Source at Argonne National Laboratory is supported by the U.S. DOE Contract No. DE-AC02-06CH11357.

REFERENCES AND NOTES

1. Huh, C.; Scriven, L. E. Hydrodynamic Model of Steady Movement of a Solid/Liquid/Fluid Contact Line. *J. Colloid Interface Sci.* **1971**, *35*, 85–101.
2. Deegan, R. D.; Bakajin, O.; Dupont, T. F.; Huber, G.; Nagel, S. R.; Witten, T. A. Capillary Flow as the Cause of Ring Stains from Dried Liquid Drops. *Nature* **1997**, *389*, 827–829.
3. Bonn, D.; Eggers, J.; Indekeu, J.; Meunier, J.; Rolley, E. Wetting and Spreading. *Rev. Mod. Phys.* **2009**, *81*, 739–805.
4. Berteloot, G.; Pham, C. T.; Daerr, A.; Lequeux, F.; Limat, L. Evaporation-Induced Flow near a Contact Line: Consequences on Coating and Contact Angle. *Europhys. Lett.* **2008**, *83*, 14003.
5. Li, L. Q.; Gao, P.; Schuermann, K. C.; Ostendorp, S.; Wang, W. C.; Du, C. A.; Lei, Y.; Fuchs, H.; De Cola, L.; Mullen, K.; *et al.* Controllable Growth and Field-Effect Property of Monolayer to Multilayer Microstripes of an Organic Semiconductor. *J. Am. Chem. Soc.* **2010**, *132*, 8807–8809.

6. Li, L.; Koepf, M. H.; Gurevich, S. V.; Friedrich, R.; Chi, L. Structure Formation by Dynamic Self-Assembly. *Small* **2012**, *8*, 488–503.
7. Li, L. Q.; Gao, P.; Wang, W. C.; Mullen, K.; Fuchs, H.; Chi, L. F. Growth of Ultrathin Organic Semiconductor Microstripes with Thickness Control in the Monolayer Precision. *Angew. Chem., Int. Ed.* **2013**, *52*, 12530–12535.
8. Paxson, A. T.; Varanasi, K. K. Self-Similarity of Contact Line Depinning from Textured Surfaces. *Nat. Commun.* **2013**, *4*, 1492.
9. Xu, X.; Vereecke, G.; Chen, C.; Pourtois, G.; Armini, S.; Verellen, N.; Tsai, W.-K.; Kim, D.-W.; Lee, E.; Lin, C.-Y.; *et al.* Capturing Wetting States in Nanopatterned Silicon. *ACS Nano* **2014**, *8*, 885–893.
10. Checco, A.; Ocko, B.; Rahman, A.; Black, C.; Tasinkevych, M.; Dietrich, S. Collapse and Reversibility of the Superhydrophobic State on Nanotextured Surfaces. *Phys. Rev. Lett.* **2014**, *112*, 216101.
11. Diguet, A.; Le Berre, M.; Chen, Y.; Baigl, D. Preparation of Phospholipid Multilayer Patterns of Controlled Size and Thickness by Capillary Assembly on a Microstructured Substrate. *Small* **2009**, *5*, 1661–1666.
12. Sele, C. W.; Kjellander, B. K. C.; Niesen, B.; Thornton, M. J.; van der Putten, J. B. P. H.; Myny, K.; Wondergem, H. J.; Moser, A.; Resel, R.; van Breemen, A. J. J. M.; *et al.* Controlled Deposition of Highly Ordered Soluble Acene Thin Films: Effect of Morphology and Crystal Orientation on Transistor Performance. *Adv. Mater.* **2009**, *21*, 4926–4931.
13. Li, M. M.; An, C. B.; Pisula, W.; Mullen, K. Alignment of Organic Semiconductor Microstripes by Two-Phase Dip-Coating. *Small* **2014**, *10*, 1926–1931.
14. Chen, X. D.; Hirtz, M.; Fuchs, H.; Chi, L. F. Self-Organized Patterning: Regular and Spatially Tunable Luminescent Submicrometer Stripes over Large Areas. *Adv. Mater.* **2005**, *17*, 2881–2885.
15. Fang, H.-W.; Li, K.-Y.; Su, T.-L.; Yang, T. C.-K.; Chang, J.-S.; Lin, P.-L.; Chang, W.-C. Dip Coating Assisted Polylactic Acid Deposition on Steel Surface: Film Thickness Affected by Drag Force and Gravity. *Mater. Lett.* **2008**, *62*, 3739–3741.
16. Le Berre, M.; Chen, Y.; Baigl, D. From Convective Assembly to Landau–Levich Deposition of Multilayered Phospholipid Films of Controlled Thickness. *Langmuir* **2009**, *25*, 2554–2557.
17. Rogowski, R. Z.; Darhuber, A. A. Crystal Growth near Moving Contact Lines on Homogeneous and Chemically Patterned Surfaces. *Langmuir* **2010**, *26*, 11485–11493.
18. Doumenc, F.; Guerrier, B. Self-Patterning Induced by a Solutal Marangoni Effect in a Receding Drying Meniscus. *Europhys. Lett.* **2013**, *103*, 14001.
19. Huang, J. X.; Kim, F.; Tao, A. R.; Connor, S.; Yang, P. D. Spontaneous Formation of Nanoparticle Stripe Patterns through Dewetting. *Nat. Mater.* **2005**, *4*, 896–900.
20. Kraus, T.; Malaquin, L.; Schmid, H.; Riess, W.; Spencer, N. D.; Wolf, H. Nanoparticle Printing with Single-Particle Resolution. *Nat. Nanotechnol.* **2007**, *2*, 570–576.
21. Colosqui, C. E.; Morris, J. F.; Stone, H. A. Hydrodynamically Driven Colloidal Assembly in Dip Coating. *Phys. Rev. Lett.* **2013**, *110*, 188302.
22. Small, D. M., Ed. *The Physical Chemistry of Lipids: From Alkanes to Phospholipids (Handbook of Lipid Research)*; Plenum Press: New York, 1986.
23. Sirota, E. B.; King, H. E.; Singer, D. M.; Shao, H. H. Rotator Phases of the Normal Alkanes: An X-ray-Scattering Study. *J. Chem. Phys.* **1993**, *98*, 5809–5824.
24. Wu, X. Z.; Sirota, E. B.; Sinha, S. K.; Ocko, B. M.; Deutsch, M. Surface Crystallization of Liquid Normal Alkanes. *Phys. Rev. Lett.* **1993**, *70*, 958.
25. Wu, X. Z.; Ocko, B. M.; Sirota, E. B.; Sinha, S. K.; Deutsch, M.; Cao, B. H.; Kim, M. W. Surface Tension Measurements of Surface Freezing in Liquid Normal Alkanes. *Science* **1993**, *261*, 1018.
26. Ocko, B. M.; Wu, X. Z.; Sirota, E. B.; Sinha, S. K.; Gang, O.; Deutsch, M. Surface Freezing in Chain Molecules: Normal Alkanes. *Phys. Rev. E* **1997**, *55*, 3164–3182.
27. Pfohl, T.; Mohwald, H.; Riegler, H. Ellipsometric Study of the Wetting of Air/Water Interfaces with Hexane, Heptane, and Octane from Saturated Alkane Vapors. *Langmuir* **1998**, *14*, 5285–5291.
28. Cisternas, E. A.; Corrales, T. P.; del Campo, V.; Soza, P. A.; Volkmann, U. G.; Bai, M. J.; Taub, H.; Hansen, F. Y. Crystalline-to-Plastic Phase Transitions in Molecularly Thin *n*-Dotriacontane Films Adsorbed on Solid Surfaces. *J. Chem. Phys.* **2009**, *131*, 114705.
29. Huber, P.; Wallacher, D.; Albers, J.; Knorr, K. Quenching of Lamellar Ordering in an *n*-Alkane Embedded in Nanopores. *Europhys. Lett.* **2004**, *65*, 351.
30. Henschel, A.; Hofmann, T.; Huber, P.; Knorr, K. Preferred Orientations and Stability of Medium Length *n*-Alkanes Solidified in Mesoporous Silicon. *Phys. Rev. E* **2007**, *75*, 021607.
31. Gruener, S.; Huber, P. Spontaneous Imbibition Dynamics of an *n*-Alkane in Nanopores: Evidence of Meniscus Freezing and Monolayer Sticking. *Phys. Rev. Lett.* **2009**, *103*, 174501.
32. Kusmin, A.; Gruener, S.; Henschel, A.; Holderer, O.; Allgaier, J.; Richter, D.; Huber, P. Evidence of a Sticky Boundary Layer in Nanochannels: A Neutron Spin Echo Study of *n*-Hexatriacontane and Poly(ethylene oxide) Confined in Porous Silicon. *J. Phys. Chem. Lett.* **2010**, *1*, 3116–3121.
33. Fu, D.; Su, Y.; Gao, X.; Liu, Y.; Wang, D. Confined Crystallization of *n*-Hexadecane Located inside Microcapsules or outside Submicrometer Silica Nanospheres: A Comparison Study. *J. Phys. Chem. B* **2013**, *117*, 6323–6329.
34. Volkmann, U. G.; Pino, M.; Altamirano, L. A.; Taub, H.; Hansen, F. Y. High-Resolution Ellipsometric Study of an *n*-Alkane Film, Dotriacontane, Adsorbed on a SiO_2 Surface. *J. Chem. Phys.* **2002**, *116*, 2107.
35. Yeganeh, M. S. Phase Transitions at *n*-Alkane/Solid Interfaces. *Phys. Rev. E* **2002**, *66*, 041607.
36. Askadskaya, L.; Rabe, J. P. Anisotropic Molecular-Dynamics in the Vicinity of Order–Disorder Transitions in Organic Monolayers. *Phys. Rev. Lett.* **1992**, *69*, 1395–1398.
37. Rawat, D. S.; Migone, A. D. Non-monotonic Kinetics of Alkane Adsorption on Single-Walled Carbon Nanotubes. *J. Phys. Chem. C* **2012**, *116*, 975–979.
38. Schollmeyer, H.; Ocko, B.; Riegler, H. Surface Freezing of Triacontane at SiOx/Air Interfaces: Submonolayer Coverage. *Langmuir* **2002**, *18*, 4351–4355.
39. Schollmeyer, H.; Struth, B.; Riegler, H. Long Chain *n*-Alkanes at SiO_2/Air Interfaces: Molecular Ordering, Annealing, and Surface Freezing of Triacontane in the Case of Excess and Submonolayer Coverage. *Langmuir* **2003**, *19*, 5042.
40. Mo, H.; Taub, H.; Volkmann, U. G.; Pino, M.; Ehrlich, S. N.; Hansen, F. Y.; Lu, E.; Miceli, P. A Novel Growth Mode of Alkane Films on a SiO_2 Surface. *Chem. Phys. Lett.* **2003**, *377*, 99–105.
41. Bai, M.; Knorr, K.; Simpson, M. J.; Trogisch, S.; Taub, H.; Ehrlich, S. N.; Mo, H.; Volkmann, U. G.; Hansen, F. Y. Nanoscale Observation of Delayering in Alkane Films. *Europhys. Lett.* **2007**, *79*, 26003.
42. Riegler, H.; Koehler, R. How Pre-melting on Surrounding Interfaces Broadens Solid–Liquid Phase Transitions. *Nat. Phys.* **2007**, *3*, 890.
43. Bai, M.; Trogisch, S.; Magonov, S.; Taub, H. Explanation and Correction of False Step Heights in Amplitude Modulation Atomic Force Microscopy Measurements on Alkane Films. *Ultramicroscopy* **2008**, *108*, 946–952.
44. Lu, L. B.; Zander, K. J.; Cai, Y. G. Stability of the Parallel Layer during Alkane Spreading and the Domain Structures of the Standing-up Layer. *Langmuir* **2010**, *26*, 5624–5631.
45. Weber, C.; Frank, C.; Bommel, S.; Rukat, T.; Leitenberger, W.; Schafer, P.; Schreiber, F.; Kowarik, S. Chain-Length Dependent Growth Dynamics of *n*-Alkanes on Silica Investigated by Energy-Dispersive X-ray Reflectivity *in Situ* and in Real-Time. *J. Chem. Phys.* **2012**, *136*, 204709.
46. del Campo, V.; Cisternas, E.; Taub, H.; Vergara, I.; Corrales, T.; Soza, P.; Volkmann, U. G.; Bai, M.; Wang, S. K.; Hansen, F. Y.; *et al.* Structure and Growth of Vapor-Deposited *n*-Dotriacontane Films Studied by X-ray Reflectivity. *Langmuir* **2009**, *25*, 12962.

47. Trogisch, S.; Simpson, M. J.; Taub, H.; Volkmann, U. G.; Pino, M.; Hansen, F. Y. Atomic Force Microscopy Measurements of Topography and Friction on Dotriacontane Films Adsorbed on a SiO_2 Surface. *J. Chem. Phys.* **2005**, *123*, 154703.
48. Mo, H.; Trogisch, S.; Taub, H.; Ehrlich, S. N.; Volkmann, U. G.; Hansen, F. Y.; Pino, M. Studies of the Structure and Growth Mode of Dotriacontane Films by Synchrotron X-ray Scattering and Molecular Dynamics Simulations. *J. Phys.: Condens. Matter* **2004**, *16*, S2905–S2910.
49. Diama, A.; Matthies, B.; Herwig, K. W.; Hansen, F. Y.; Criswell, L.; Mo, H.; Bai, M.; Taub, H. Structure and Phase Transitions of Monolayers of Intermediate-Length *n*-Alkanes on Graphite Studied by Neutron Diffraction and Molecular Dynamics Simulation. *J. Chem. Phys.* **2009**, *131*, 084707.
50. Smilgies, D.-M. Scherrer Grain-Size Analysis Adapted to Grazing-Incidence Scattering with Area Detectors. *J. Appl. Crystallogr.* **2009**, *42*, 1030–1034.
51. Volkmann, U.; *et al.* unpublished.
52. Landau, L.; Levich, B. *Acta Physicochim. URSS* **1942**, *17*, 42.
53. Deryaguin, B. *Acad. Sci. URSS* **1943**, *39*, 1.
54. De Gennes, P. G. Deposition of Langmuir–Blodgett Layers. *Colloid Polym. Sci.* **1986**, *264*, 463–465.
55. Eggers, J. Hydrodynamic Theory of Forced Dewetting. *Phys. Rev. Lett.* **2004**, *93*, 094502.
56. Eggers, J. Existence of Receding and Advancing Contact Lines. *Phys. Fluids* **2005**, *17*, 082106.
57. de Gennes, P. G.; Brochard-Wyart, F.; Quere, D. *Capillarity and Wetting Phenomena: Drops, Bubbles, Pearls, Waves*; Springer: New York, 2004.
58. Ingram, B. T. Wetting of Silica by *n*-Alkanes. *J. Chem. Soc., Faraday Trans. 1* **1974**, *70*, 868–876.
59. Langer, J. S. Instabilities and Pattern-Formation in Crystal-Growth. *Rev. Mod. Phys.* **1980**, *52*, 1–28.
60. Wurger, A. Molecular Ordering in Amphiphile Monolayers and Alkanes. *Phys. Rev. Lett.* **1999**, *83*, 4816–4819.
61. Mukherjee, P. K.; Deutsch, M. Landau Theory of the R-II-R-I-R-V Rotator Phases of Alkanes. *Phys. Rev. B* **1999**, *60*, 3154–3162.
62. Wurger, A. Rotator Phases and Herringbone Order in Langmuir Monolayers and Alkanes. *J. Chem. Phys.* **2000**, *112*, 3897–3908.
63. Libbrecht, K. G. The Physics of Snow Crystals. *Rep. Prog. Phys.* **2005**, *68*, 855–895.
64. Esselink, K.; Hilbers, P. A. J.; VanBeest, B. W. H. Molecular-Dynamics Study of Nucleation and Melting of *n*-Alkanes. *J. Chem. Phys.* **1994**, *101*, 9033–9041.
65. Fujiwara, S.; Sato, T. Molecular Dynamics Simulation of Structural Formation of Short Polymer Chains. *Phys. Rev. Lett.* **1998**, *80*, 991–994.
66. Waheed, N.; Ko, M. J.; Rutledge, G. C. Molecular Simulation of Crystal Growth in Long Alkanes. *Polymer* **2005**, *46*, 8689–8702.
67. Anwar, M.; Turci, F.; Schilling, T. Crystallization Mechanism in Melts of Short *n*-Alkane Chains. *J. Chem. Phys.* **2013**, *139*, 214904.
68. Deegan, R. D.; Bakajin, O.; Dupont, T. F.; Huber, G.; Nagel, S. R.; Witten, T. A. Contact Line Deposits in an Evaporating Drop. *Phys. Rev. E* **2000**, *62*, 756–765.
69. Cazabat, A. M.; Heslots, F.; Troian, S. M.; Carles, P. Fingering Instability of Thin Spreading Films Driven by Temperature-Gradients. *Nature* **1990**, *346*, 824–826.
70. Cazabat, A. M.; Heslot, F.; Carles, P.; Troian, S. M. Hydrodynamic Fingering Instability of Driven Wetting Films. *Adv. Colloid Interface Sci.* **1992**, *39*, 61–75.
71. Baeumchen, O.; Marquant, L.; Blossey, R.; Muench, A.; Wagner, B.; Jacobs, K. Infuence of Slip on the Rayleigh-Plateau Rim Instability in Dewetting Viscous Films. *Phys. Rev. Lett.* **2014**, *113*, 014501.
72. Vuilleumier, R.; Ego, V.; Neltner, L.; Cazabat, A. M. Tears of Wine: The Stationary State. *Langmuir* **1995**, *11*, 4117–4121.
73. Huppert, H. E. Flow and Instability of a Viscous Current Down a Slope. *Nature* **1982**, *300*, 427–429.
74. Sur, J.; Witelski, T. P.; Behringer, R. P. Steady-Profile Fingering Flows in Marangoni Driven Thin Films. *Phys. Rev. Lett.* **2004**, *93*, 247803.
75. Tidswell, I. M.; Ocko, B. M.; Pershan, P. S.; Wasserman, S. R.; Whitesides, G. M.; Axe, J. D. X-ray Specular Reflection Studies of Silicon Coated by Organic Monolayers (Alkylsiloxanes). *Phys. Rev. B* **1990**, *41*, 1111–1128.
76. Chang, S. S.; Maurey, J. R.; Pummer, W. J. Solubilities of Two *n*-Alkanes in Various Solvents. *J. Chem. Eng. Data* **1983**, *28*, 187–189.